Quantum Shells Boost the Optical Gain of Lasing Media.

James Cassidy,[1] Benjamin T. Diroll,[2] Navendu Mondal,[3] David B. Berkinsky,[4] Kehui Zhang,[3] Dulanjan Harankahage,[1] Dmitry Porotnikov,[1] Reagan Gately,[5] Dmitriy Khon,[5] Andrew H. Proppe,[4] Moungi G. Bawendi,[4] Richard D. Schaller,[2,6] Anton V. Malko,[3] Mikhail Zamkov.[1]*

The Center for Photochemical Sciences and Department of Physics, Bowling Green State University, Bowling Green, Ohio 43403.[1] Center for Nanoscale Materials, Argonne National Laboratory, Lemont, Illinois 60439.[2] Department of Physics, University of Texas at Dallas, Richardson, Texas 75080.[3] Department of Chemistry, Massachusetts Institute of Technology, 77 Massachusetts Avenue, Cambridge, Massachusetts 02139,[4] Department of Chemistry and Biochemistry, St. Mary's University, San Antonio, Texas, 78228,[5] Department of Chemistry, Northwestern University, Evanston, Illinois 60208.[6]

Corresponding author: zamkovm@bgsu.edu; Tel: 419-372-0264; Fax: 419-372-9938

Abstract. Auger decay of multiple excitons represents a significant obstacle to photonic applications of semiconductor quantum dots (QDs). This non-radiative process is particularly detrimental to the performance of QD-based electroluminescent and lasing devices. Here, we demonstrate that semiconductor quantum shells with an "inverted" QD geometry inhibit Auger

recombination, allowing substantial improvements to their multi-exciton characteristics. By promoting a spatial separation between multiple excitons, the quantum shell geometry leads to ultralong biexciton lifetimes (>10 ns) and a large biexciton quantum yield. Furthermore, the architecture of quantum shells induces an exciton-exciton repulsion, which splits exciton and biexciton optical transitions, giving rise to Auger-inactive single-exciton gain mode. In this regime, quantum shells exhibit the longest optical gain lifetime reported for colloidal QDs to date (> 6 ns), which makes this geometry an attractive candidate for the development of optically- and electrically-pumped gain media.

KEYWORDS: *nanocrystal, X-ray, light, scintillator, laser diode, biexciton, trion.*

INTRODUCTION

Colloidal semiconductor quantum dots (QDs) hold strong promise for future optoelectronic applications.[1,2] These nanomaterials are inexpensive to process and offer a broad range of attractive quantum-mechanical properties. Central to their appeal is an efficient, narrowband emission,[3] which has encouraged QD commercialization in backlit displays.[4,5] Meanwhile, a combination of high color purity, quantized electronic levels, and solution-phase device processing has stimulated the interest in QD-based optically and electrically pumped light-emitting devices.[6,7] In this case, QDs can offer low lasing thresholds and temperature-insensitive gains,[8-11] a tunable electroluminescent spectrum,[12,13] and low injection current in high-brightness LEDs.[14-16]

The geometric confinement of electrical charges in colloidal QDs leads to extraordinary optical performance in a single-exciton regime, but is detrimental to multi-exciton dynamics. The Coulomb interactions of proximal excitons cause their Auger recombination,[17] which leads to substantial energy losses in photonic applications.[18,19] Accordingly, several strategies have been devised over the years for suppressing Auger processes in colloidal semiconductor QDs. The most straightforward approach is to expand the volume occupied by photoinduced charges, which leads

to a proportional increase in the Auger lifetime. This is usually achieved by using 1D-2D nanoparticle geometries, such as 1D nanorods[20] or 2D nanoplatelets,[21-24] where biexciton lifetimes scale super-linearly with the volume, or nanostructures where one of the carriers delocalizes into the bulk (e.g. giant CdSe/CdS core-shell QDs).[25-27] Recently, another type of colloidal nanocrystals, known as nanoshell QDs or quantum shells, [28-30] has emerged as a promising candidate for the suppression of Auger decay. These nanomaterials disperse multiple excitons across a spherical shell layer, and, therefore, can support longer multi-exciton lifetimes. Unfortunately, the synthetic challenges associated with the colloidal fabrication of these layered QDs have previously hindered their optical-gain performance.[31,32]

Here, we demonstrate that semiconductor quantum shells fabricated *via* the colloidal epitaxy approach enable strong suppression of Auger recombination, resulting in the longest optical gain reported for colloidal semiconductor QDs to date (Table S1). The "inverted" architecture of quantum shells, featuring a CdS_{bulk}-CdSe-CdS core-shell-shell composition, benefits from the repulsion of multiple excitons in a CdSe quantum-well layer (Figure 1a). Under these conditions, the exciton-exciton (X-X) Auger recombination nearly vanishes, giving rise to ultralong biexciton lifetimes (Table S2) with an associated biexciton quantum yield of 81%. In addition, the presence of the X-X repulsion in CdS_{bulk}-CdSe-CdS quantum shells causes optical transparency at the single-exciton band, permitting the Auger-invariant, single-exciton[33] stimulated emission. The single-exciton optical gain mechanism was attributed to a ~ 57-meV blue-shift of the second photon absorbing transition[34,35] (Figure 1b). The coexistence of single and double exciton gain modes offered important advantages of a broad amplification bandwidth (~ 300 meV) and the long gain lifetime (~ 6.5 ns). The nature of X-X interactions in quantum shells and the underlying Auger suppression were explained within the effective mass approximation. Our calculations show that quantum shells support an intrinsically smaller electron-hole overlap

compared to “conventional” CdSe-CdS core-shell QDs, which diminishes their non-radiative recombination rate.

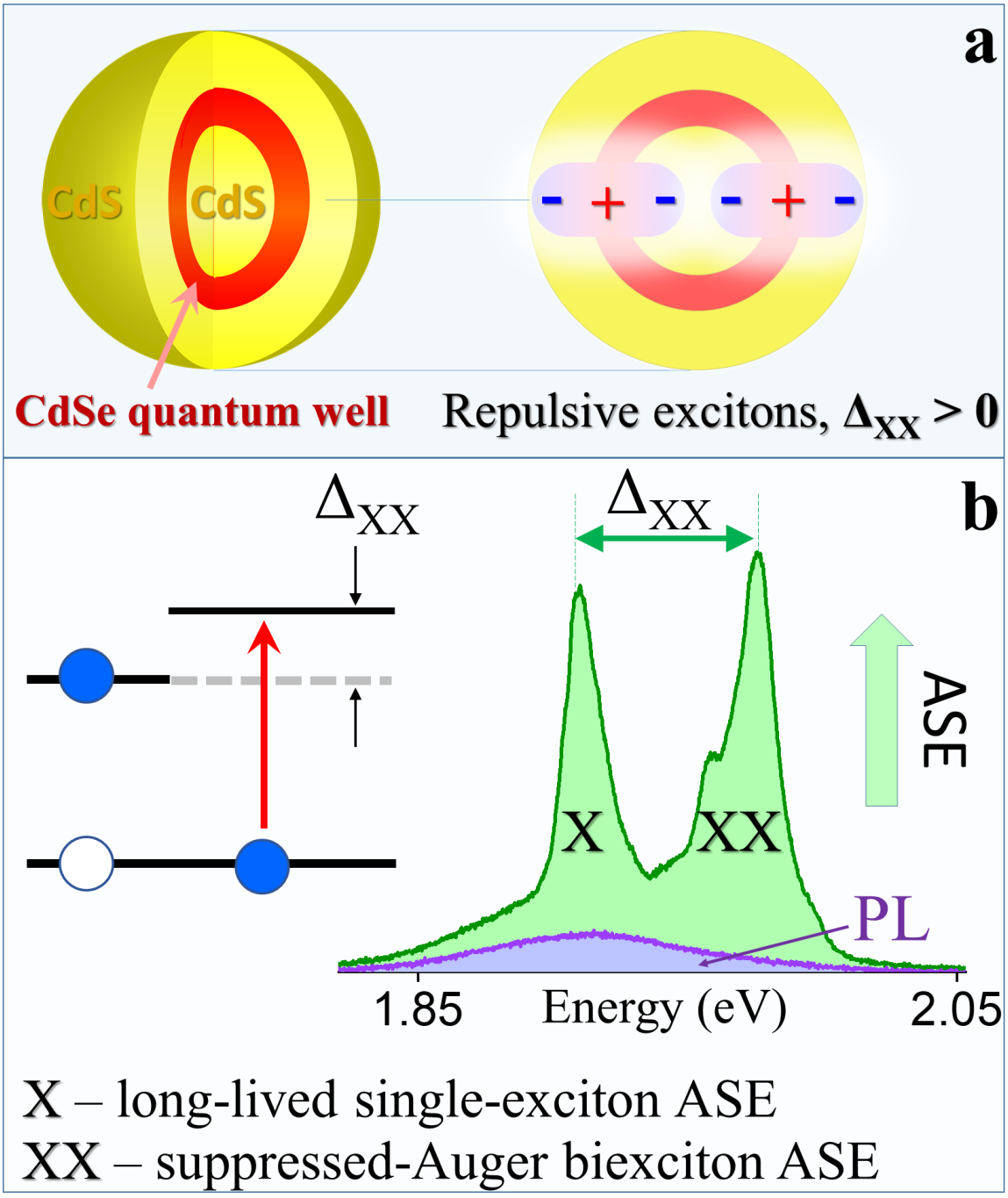

Figure 1. (a). The geometry of a quantum shell. A spherical core-shell-shell structure features a two-dimensional quantum-confined CdSe layer, sandwiched between the bulk-size CdS core and the surface CdS shell components (Figures S1, S2). The strong localization of photoinduced holes in the CdSe domain leads to the repulsion of multiple excitons ($\Delta_{XX} > 0$). (b). The X-X repulsion

offsets an absorbing transition energy for the second incoming photon, allowing for a single-exciton optical gain in quantum shells. The spectrum shows a dual-mode amplified spontaneous emission (ASE) involving both the single-exciton and the biexciton gain mechanisms. These bands are separated by the X-X interaction energy of 57 meV. The pump fluence was 10.5 $\mu J/cm^2$.

RESULTS AND DISCUSSION

The geometry of a CdS_{bulk}-CdSe-CdS quantum shell is illustrated in Figure 1a. The CdSe quantum-well layer is sandwiched between the two CdS "barrier" components, providing a potential energy minimum to photoinduced charges. An important aspect of the quantum shell design is the large-diameter CdS core domain, which distinguishes the present quantum shell geometry from previously reported Quantum-Dot Quantum-Wells (QDQW).[36-42] The existence of a large core increases the volume occupied by multiple excitons, leading to their reduced Coulomb interactions. This results in the reduction of the Auger recombination rate, which is inversely proportional to the nanoparticle volume, ($\Gamma^{-1} \sim V^{1.1}$).[43,44]

In the present work, CdS_{bulk}-CdSe-CdS quantum shells were fabricated by growing two sequential shell layers onto 4.5 - 6.0 nm CdS core nanocrystals. The size of the CdS core component surpasses the CdS exciton Bohr radius (~3.4 nm)[45] and therefore is considered to be bulk-like. An improved growth strategy, called colloidal epitaxy, was used to achieve defect-free interfaces between a thin CdSe quantum-well layer and bulk-like CdS phases, which was crucial to suppressing Auger recombination of multiple excitons. The deposition of the ~2-nm CdSe shell onto the CdS core results in the band gap photoluminescence (PL) (Figures 2a and S3), which intensity increases with the subsequent growth of the 3-5 nm CdS "surface-barrier" shell. In the case of 4.5-nm-core quantum shells, the diameter of the entire nanoparticle averages 16 nm with a size dispersion of 8.1% (Figures 2d-2f and S6), whereas 6.0-nm-core quantum shells reach an average size of 22 nm (Figure 2g). The estimated 2.0-nm thickness of the CdSe quantum-well layer in 6.0-nm-core nanostructures was corroborated by the spectral position of their respective PL maximum (Figure SF11). The presence of the CdSe quantum-well layer was also evident through a color-contrast in high angle annular dark field (HAADF)-STEM images (Figure S5).

The PL spectrum of 4.5-nm-core quantum shells in Figure 2a exhibits a single emission peak with a corresponding quantum yield (QY) of 52% (Figure S7). A relatively small PL linewidth (ΔE = 69 meV) in 4.5-nm-core quantum shells attests to the narrow distribution of the CdSe layer

thickness. Notably, the absorption profile of 4.5-nm-core quantum shells (Figure 2a) resembles those of high-quality CdSe-CdS core-shell QDs featuring well-resolved 1S light-hole and heavy-hole transitions. The comparison of PL intensity decay in 4.5-nm-core quantum shells measured at low and high pump fluences (<N> ≈ 0.05 and <N> ≈ 1.2 excitations per dot, respectively) reveals a long ensemble-averaged biexciton lifetime of τ_{xx} = 5.1 ns (Figure 2b, red curve). This result was corroborated by single-particle measurements of the same sample, showing an intensity-resolved characteristic biexciton lifetime of τ_{xx} = 6.2 ns (Figure S4b). Quantum shells featuring a larger, 6.0-nm core size, exhibit even longer τ_{xx}, approaching 10.5 ns (Figure S8b). To the best of our knowledge, these are among the longest biexciton lifetimes reported for colloidal semiconductor QDs to date (Table T2).

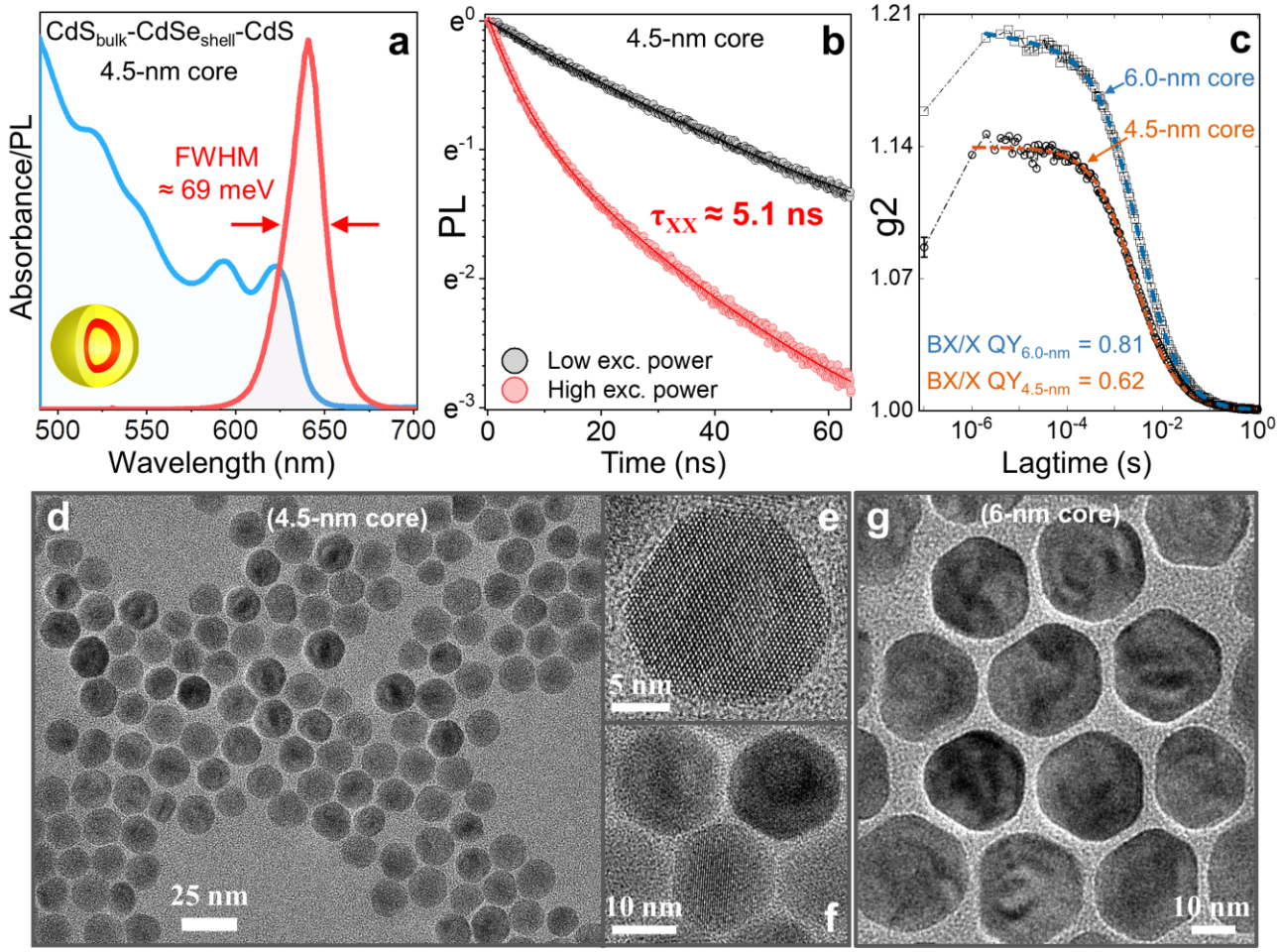

Figure 2. (a). Absorption and emission spectra of 4.5-nm-core CdS$_{bulk}$-CdSe-CdS quantum shells (R_{CdS} = 2.25 nm, H_{Se} = 2 nm and H_S = 3.75 nm). (b). The photoluminescence intensity decay of 4.5-nm-core CdS$_{bulk}$-CdSe-CdS quantum shells measured under two excitation regimes with the average number of absorbed photons per QD being equal to <N> ≈ 0.05 (grey curve) and <N> ≈ 1.2 (red curve). The high-power excitation regime reveals an ensemble-averaged biexciton lifetime

of τ_{XX} = 5.1 ns. The low-power excitation measurement (black curve) shows a single-exponential decay with an exciton lifetime of τ_{XX} = 36 ns (R-value = 0.998). (c). Lagtime-dependence of the cross-correlation function, g2, showing the ratio of biexciton to exciton QY (BX/X QY) for 4.5-nm core (orange curve) and 6.0-nm core (blue curve) quantum shells. (d). Transmission electron microscopy (TEM) image of 4.5-nm-core CdS_{bulk}-CdSe-CdS quantum shells. (e-f). High-resolution TEM images of 4.5-nm-core CdS_{bulk}-CdSe-CdS quantum shells. (g). TEM image of 6.0-nm-core CdS_{bulk}-CdSe-CdS quantum shells.

The quantum yield (QY) of biexciton emission can be expressed using statistical considerations as $QY_{XX} = 4\tau_{XX}/\tau_{rad,X}$, where τ_{XX} is the experimental biexciton lifetime and $\tau_{rad,X}$ is the radiative lifetime of single excitons.[1] Taking into account the single-exciton quantum yield QY_X = 52% and PL lifetime τ_X = 36 ns, we can estimate the biexciton-to-exciton quantum yield ratio, $QY_{XX}/QY_X = 4\tau_{XX}/(QY_X \times \tau_{rad,X}) = 4\tau_{XX}/\tau_X \approx 0.57$. To obtain a more accurate estimate of QY_{XX}, we use Fluorescence Correlation Spectroscopy that determines the ensemble averaged biexciton-to-exciton quantum yield ratio from a solution-phase photon correlation.[46] To this end, we detect emission from diffusing nanoparticles in solution using a confocal microscope and a pulsed excitation source in a Hanbury-Brown-Twiss setup. We then calculate the second order cross-correlation function, $g^{(2)}(\tau)$, according to the protocol on page S14 of the SI section. Figure 2c shows that the QY_{XX}/QY_X is higher for the 6.0-nm-core QDs (81.8% ± 1.1%) compared to 4.5-nm core samples (62.0% ± 0.4%) suggesting a reduction in the non-radiative Auger recombination pathway as a result of the greater delocalization of the electron wave function.

To understand the spectral and temporal characteristics of the optical gain in quantum shells, we performed femtosecond transient absorption (TA) measurements of dilute nanoparticle solutions. The TA study primarily focused on 4.5-nm-core quantum shells, exhibiting 80% greater single-exciton QY than those with a 6.0-nm core. In these experiments, the absorption change ($\Delta\alpha=\alpha-\alpha_0$) induced by a femtosecond pulse is monitored by using a broadband pulse of a white-light continuum. Optical gain is realized when $-\Delta\alpha/\alpha_0 > 1$, where α_0 is a linear absorption.

Figure 3a shows the non-linear absorption spectra for 4.5-nm-core quantum shells, expressed in terms of number of electron-hole pairs, $\langle N_{eh}\rangle = f\sigma$, where f is the excitation fluence and σ = 2.3×10^{-13} cm^2 is single quantum shell's absorption cross-section.[47] Absorption cross-section is calculated using the standard analysis presented in Ref. 47. It is evident that at lowest excitation powers, the gain region ($\alpha<0$) appears at the single exciton (X) transition, corresponding to the

spectral position of the PL maximum. Upon the increase of the excitation fluence, the gain region considerably broadens to include biexcitons (BX) at ~ 620 nm (2.02 eV).

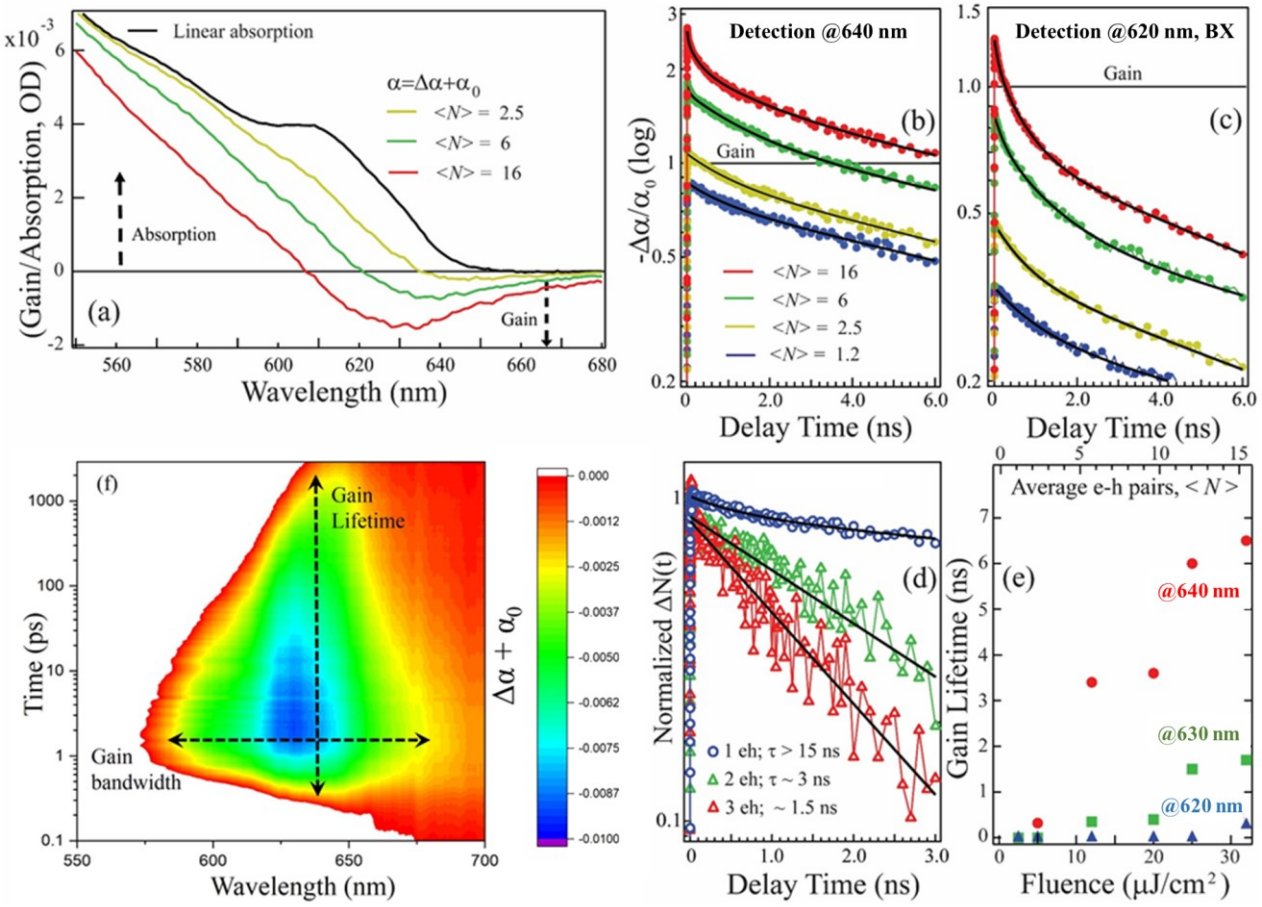

Figure 3. (a) Pump-dependent optical gain development in the non-linear optical absorption spectra of 4.5-nm-core CdS_{bulk}-CdSe-CdS quantum shells. Positive values on the left scale indicate absorption, negative–gain. Black solid line – linear absorption spectrum. Spectra are recorded at 2 ps delay. (b, c) Population-dependent TA dynamics at various photon energies. Black solid lines – single/double/triple exponential fits (d) Dynamics of 1, 2 and 3 e-h pair states obtained using the subtractive procedure as described in the text. Black lines - single exponential fits. Here, larger core sample (6 nm) is used. (e) Gain lifetimes at different wavelengths extracted from dynamics in panels (b) – red dots, (c) –blue triangles and additional set at 630 nm – green squares (f). A 3D lifetime/bandwidth contour plot of the optical gain in a low-concentration, 4.5-nm-core quantum shells. The positive gain is achieved when $\alpha + \alpha\Delta > 0$. The pump fluence is 36 μJ/cm^2.

Figure 3 (b,c) shows gain dynamics at X and BX transitions. Dynamics of X transition at the lowest excitation level are close to the monoexponential with τ_{long}>15 ns, with more precise

determination limited by the scanning range of the delay line. Optical gain ($-\Delta\alpha/\alpha_0 > 1$) appears close to $\langle N_{eh} \rangle \sim 2$ and extends to $\tau_{gain} \sim 6.5$ ns (Figure 3e) at the highest excitation level, making it the longest gain lifetime recorded for colloidal semiconductor QDs to date. For a comparison, first reports of optical gain in colloidal CdSe/ZnS QDs dealt with exciton gain lifetimes in 10-100 ps range as they were limited by strong Auger recombination.[48-50] More recently, long–lived optical gain has been achieved in CdSe-CdS nanoplatelets (830 ps)[51] and charged CdSe-CdS QDs (1.6 ns),[52] where enhanced lifetimes were possible due to sub-single exciton gain mechanisms.

Gain at the BX transition develops at the higher excitation levels, nevertheless reaching ~300 ps lifetime. We note that the power dependence of X and BX gain thresholds has a complex character imposed by the multi-exciton interactions in the initially populated state, which alters $\langle N_{eh} \rangle$ from the values derived using population statistics.[53-55] These multi-exciton interactions affect both the gain threshold and gain bandwidth. The latter is illustrated in Figure 3f showing the 3D bandwidth/lifetime contour plot of the excited state absorption at a higher excitation level (fluence = 36 $\mu J/cm^2$). The gain bandwidth extends to ~ 300 meV, which is one of the largest known for colloidal QDs. Previously, large gain bandwidths have been observed in core/shell quantum dots that were capable of accommodating multi-exciton populations either by having a large optical cross section[25,56] or through energy-coupling to quantum shells.[57]

To characterize multiexcitonic Auger recombination decays, we recorded exciton population dynamics at $\langle N_{eh} \rangle = 0.5$; 1.5; and 2.5 pairs and used a simple subtractive procedure[43] to derive the single exponential decays of each multiexciton species, shown in Figure 3d. As expected, the resultant carrier dynamics become progressively faster due to Auger recombination. Ratio of Auger times for 3 and 2 pair states, $\tau_3 : \tau_2 \sim 0.5 : 1$ is approximately following the volumetric scaling that is expected for the spherically-symmetric confinement of carriers, $\tau_3 : \tau_2 \sim 0.44 : 1$.

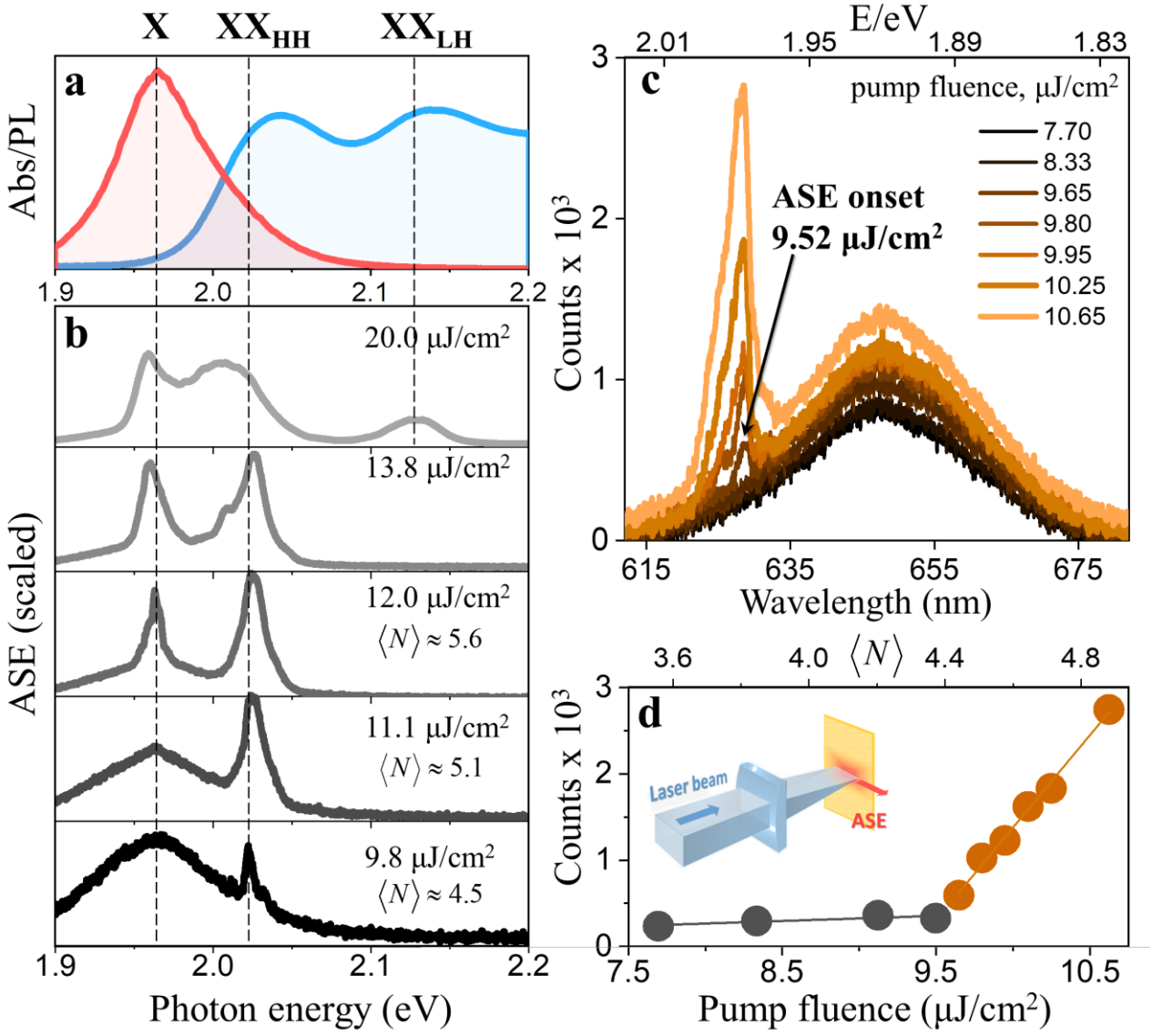

Figure 4. (a). Absorption (blue) and emission (red) spectra of 4.5-nm-core quantum shells (R_{CdS} = 2.5 nm, H_{Se} = 2 nm and H_S = 4.5 nm). (b). Emission spectra observed from thin films of 4.5-nm-core quantum shells for different pump fluences. The narrow ASE peak at 9.8 μJ/cm^2 corresponds to XX optical gain. The appearance of the lower-energy ASE feature at 11.1 μJ/cm^2 that matches the spectral position of the PL peak is attributed to a single exciton gain mechanism. <N> are the average e-h pairs. (c). Evolution of the biexciton ASE peak with increasing pump fluence. (d). The pump fluence dependence of the integrated intensity in (c), which reveals the biexciton ASE threshold of 9.52 μJ/cm^2.

The long optical gain lifetime of quantum shells makes these nanomaterials a promising candidate for the development of lasing media. To explore this prospect, we have measured the amplified spontaneous emission (ASE) from a spincoated film of 4.5-nm-core quantum shells (see

Figure 4d). According to the standard practice, the samples were excited by focusing ultrafast pulses through a cylindrical lens and the ASE was observed perpendicular to the excitation direction. The onset of ASE is evident as a spectrally narrowed peak with superlinear fluence-dependence on the higher-energy side of the broader PL band (Figure 4c). The energy difference between the steady-state PL (Figure 4a) and ASE peak (Figure 4b) suggests a biexciton origin of the optical gain mechanism with the corresponding biexciton binding energy of -57 meV (X-X repulsion). Previously, such a significant X-X repulsion has been observed only in type II QDs,[33] where electrons and holes occupy different components of a core-shell nanoparticle. Notably, the XX ASE peak of quantum shells appears at a relatively low pump fluence of 9.52 μJ/cm^2 (Figure 4c).

In addition to the XX ASE feature at E = 2.02 eV, another narrow-bandwidth ASE peak emerges when the pump fluence is increased to 11.1 μJ/cm^2 (Figure 4b). The spectral position of this ASE peak (E = 1.96 eV) matches the steady state PL, indicating a single-exciton origin of this emission. Evidence of the single-exciton gain mechanism in ASE measurements corroborates TA gain spectra in Figure 3a, which also show the optical gain maximum at the PL photon energy. The observation of the single-exciton ASE feature provides additional evidence in support of X-X repulsion, which perturbs the absorption energy of the second photon in quantum shells (Figure 1b).[34,58] The fact that biexciton ASE appears at lower fluences than a single-exciton ASE feature is partly contributed by the interaction between X and XX emissive phases. In general, the average number of excitons per nanoparticle, required for a single exciton optical gain is $\langle N^X_{gain} \rangle = 2/3$.[34] For a biexciton-mode ASE, the threshold occupancy rises to $\langle N^{XX}_{gain} \rangle \geq 1$. The interference of single and double exciton bands, however, increases the single-exciton threshold: $\left\langle N^X_{gain} \right\rangle = 2/\left(3 - \exp(-\Delta^2_{XX}/\Gamma^2)\right)$, where Γ in the inhomogenious linewidth of the lowest-energy transition. For quantum shells (Γ = 69 meV, Δ_{XX} = 57 meV), this correction yields a theoretical threshold of $\left\langle N^X_{gain} \right\rangle = 0.8$. Further suppression of the single-exciton ASE threshold will be contributed by interactions with other multi-exciton bands[57] that are clearly present in quantum shells (Figure SF10). Nevertheless, the interaction between X and other emissive phases, by itself, is not sufficient to explain the "re-ordering" of the single- and bi-exciton ASE onsets in investigated materials. According to TA measurements of the stimulated emission in Figure 3a, the X gain (λ ≈ 645 nm) develops at lower fluences that XX gain (λ ≈ 620 nm).

The question is why the single-exciton ASE feature arrears at a slightly higher fluence in solid films, despite being observed at lower fluences in TA measurements. This anomalous behavior could be attributed to the re-absorption of the X spontaneous emission in ASE measurements. In solution-phase samples (TA measurements), the reabsorption of the single-exciton emission is insignificant due to the lack of sample absorption at this wavelength. In a solid film (ASE measurements), the absorption at the single-exciton emission is no longer negligible (Figure SF12a). Such reabsorption of the emitted photon causes the suppression of optical gain, which enhances ASE threshold for a single-exciton gain mechanism. For a biexciton gain ($\lambda = 620$ nm), the absorption difference between solution and solid samples is not significant, so XX ASE feature is suppressed less due to re-absorbance than X ASE peak. In support of this explanation, we provide an example of a low-quality quantum shell film (significant amount of light scattering, Figure SF12b), where single-exciton gain is still absent at 36.0 $\mu J/cm^2$.

Further increases of the excitation fluence result in the saturation of X and XX 1S transitions, causing ASE from higher-energy excitons, including 1S(e)-2S3/2(h) (Figure 4a, top panel) and 1P(e)-1P3/2(h) (Figures S9, S10) interband transitions. We note that optical gain due to 1P excitons is rarely observed in conventional, core-shell QDs because of relatively short multiexciton lifetimes.[25] Such high-energy ASE allows demonstration of optical amplifications with a large spectral bandwidth (Figure 3f) and low excitation thresholds.

To understand the origin of the strong exciton-exciton repulsion in quantum shells, we calculate single-carrier wave functions for the lowest-energy excitons within the effective-mass approximation[59,60] (see SI for details of calculation). The corresponding electron and hole radial probabilities, $r^2R^2(r)$, are shown in Figure 5a for the three regions of a 4.5-nm-core CdS_{core}-$CdSe_{shell}$-CdS quantum shell with $R_{CdS} = 2.25$ nm, $H_{Se} = 2$ nm and $H_S = 3.75$ nm. The strong localization of photogenerated holes in the CdSe shell region leads to a vanishing probability of hole tunneling to the origin of a quantum shell QD ($r = 0$). For comparison, in case of giant, 16-nm CdSe-CdS core-shell QDs with $R_{CdSe} = 2.3$ and $H_S = 5.7$ nm, the radial probability profile of photoinduced holes is skewed towards the origin. Such a difference in the hole localization pattern between the two morphologies leads to a considerable difference is the electron-hole overlap. For CdS_{core}-CdSe-CdS quantum shells, the overlap integral (Eq. SE11) is determined to be $f = 0.185$, which is 2.5 times lower than in the case of giant core-shell QDs of the same size ($f = 0.505$). We note that a lower e-h overlap enhances X-X repulsion by favoring co-localization of same-sign

charges.[1] Simultaneously, it decreases the Coulomb attraction of excitons, since charges of opposite sign are separated across the hetero-interface. The net effect is a strong X-X repulsion, manifested in this work through blue-shifted ASE.

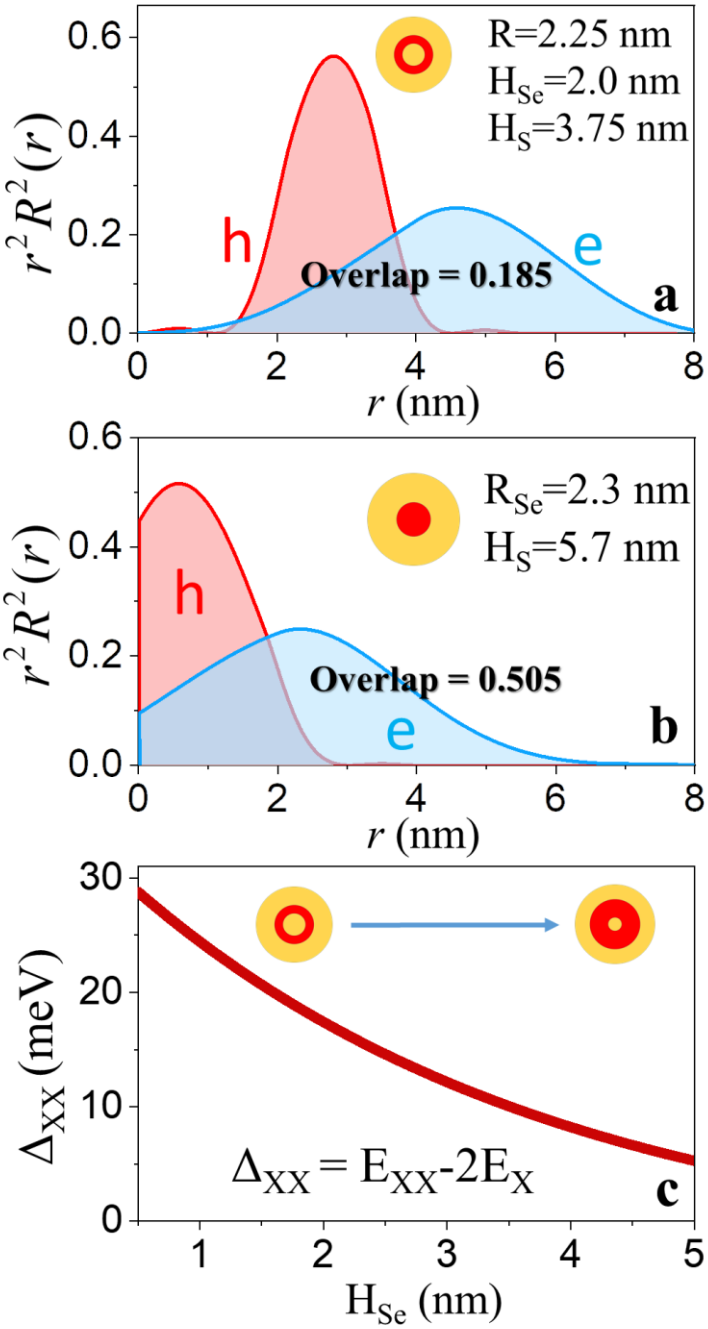

Figure 5. (a). Radial probability distributions for electron and hole wave functions in a 16-nm CdS_{bulk}-CdSe-CdS quantum shell (R_{CdS} = 2.25 nm, H_{Se} = 2 nm and H_S = 3.75 nm). The corresponding overlap integral is 0.185 (see SE11). (b). Radial probability distributions for

electron and hole wave functions in a 16-nm giant CdSe-CdS core-shell QD (R_{CdSe} = 2.3 and H_S = 5.7 nm). The corresponding overlap integral is 0.505. (c). The CdSe quantum shell thickness dependence of the X-X interaction energy, Δ_{XX}, assuming the total nanoparticle diameter of 16 nm (Eq. SE9).

A relatively low electron-hole overlap in quantum shells supports the premise of repulsive excitons.[34] A more accurate determination of the X-X interaction energy, Δ_{XX}, can be achieved by evaluating the direct Coulomb coupling between multiple electron-hole pairs.[61] To this end, we use the first-order perturbation theory to calculate the X-X coupling between two ground-state electrons and two ground-state holes. We note that the first-order contribution to Δ_{XX} vanishes in structures with a large electron-hole overlap (type I heterostructures), which usually require higher-order perturbation terms. The situation is different for quantum shells, where the overlap integral is sufficiently small to justify treatment within the first-order perturbation theory. Other contributions into Δ_{XX} include the core-shell interface polarization and self-interaction of each charge with its own image. Both of these terms are appreciably smaller than the direct Coulomb coupling and were not calculated here.[61] Using the aforementioned ansatz, we have evaluated the direct Coulomb coupling of excitons in a 16-nm CdS_{core}-CdSe-CdS quantum shell (see SI section II for details of calculation). The resulting X-X interaction energy, Δ_{XX}, is plotted in Figure 5c *versus* the CdSe layer thickness (H_{Se}). The positive sign of Δ_{XX}, indicates X-X repulsion, which increases with decreasing H_{Se}. For quantum shells investigated in this work, we estimate Δ_{XX} = 30 meV. This value is smaller than the experimentally observed repulsion energy of 57 meV. The discrepancy could be attributed to the fact that present calculations assume an isotropic angular distribution of photoinduced charges (L = 0), which does not take into account a possible hybridization of repulsive excitons. If the two excitons polarize away from each other, as schematically depicted in Figure 1a, charges of opposite sign will be further separated reducing the Coulomb attraction contribution.

The above theoretical analysis demonstrates that the key feature of quantum shells contributing to the long-lived optical gain is the shell-type geometry of the quantum-confined layer. It could be inferred from Figure 5c that a thin, two-dimensional geometry of CdSe in combination with its large surface area promote the biexciton repulsion. Similar characteristics are observed in chalcogenide nanoplatelets[51] and $CsPbI_3$ perovskite QDs.[58] The geometry of these quasi-2D

materials supports X-X repulsion, which permits the single and sub-single exciton gain mode. Compared to these types of colloidal QDs, however, quantum shells offer an increased lifetime of the optical gain. We attribute this beneficial feature to the delocalization of electrons out of the 2D CdSe quantum well into the CdS "barrier" layers, which helps reduce carrier Coulomb interactions.

CONCLUSIONS

In conclusion, we demonstrate that semiconductor quantum shells enable a near complete suppression of Auger processes, evidenced through a ~ 80% biexciton QY and ultralong biexciton lifetimes. An important feature of the quantum shell geometry is the energy-dispersive quantum well layer that induces the repulsion between multiple excitons. This leads to the suppression of Auger decay for biexciton populations and optical transparency at the single-exciton band, for which Auger decay is inactive. The single-exciton contribution into stimulated emission gives rise to the longest optical gain lifetime reported for colloidal QDs to date, while the presence of higher-order exciton gain enables a broad amplification bandwidth. Based on their multi-exciton properties, we expect quantum shells to emerge as a promising class of colloidal semiconductor nanocrystals for lasing and light-emitting applications.

METHODS

Materials. The following chemicals were used as received without further purification or modification: anhydrous acetone (99 %, Amresco), cadmium oxide (CdO, 99.95%, MilliporeSigma), anhydrous ethanol (99%, BeanTown Chemical), hexane (ACS grade, Thermo Scientific), mercaptopropyltrimethoxysilane (MPTA, 95%, MilliporeSigma), 1-octadecene (ODE, technical grade, 90%, MiliporeSigma), Octane (98%, MiliporeSigma), octanethiol (98%, TCI America), oleic acid (OA, technical grade, 90%, MiliporeSigma), oleylamine (OLAM, technical grade, 70%, MiliporeSigma), rhodamine 101 inner salt (R101, 94%, pure, Thermo Scientific), selenium powder (Se, 99.5%, 200 mesh, Thermo Scientific), sulfur powder (S, 99.999%, Thermo Scientific), toluene (99.8%, MiliporeSigma), and tir-n-octylphosphine (TOP, 97%, Strem Chemical).

Synthesis of 4.5-nm CdS nanocrystals. The synthesis of 4.5 nm CdS was adapted from the literature.[62] Briefly, 300 mg of CdO, 10 mL of ODE, and 10 mL of OA were loaded into a 50 mL round bottom flask. Using a Schlenk line, the flask was placed under argon and heated to 260 °C until clear. At 260 °C, a sulfur solution (90 mg sulfur powder dissolved in 5 mL ODE at 120 °C) was swiftly injected into the Cd flask. After 10 seconds of cooking, the reaction was quenched by placing the flask in a water bath. The resulting nanocrystals were precipitated 3 times using toluene/ethanol mixture and redispersed in hexane.

Synthesis of 6-nm bulk-size CdS nanocrystals. CdS NCs ("bulk" size) were synthesized according to a previously published coalescence-based growth procedure.[63] In brief, 5 mL OLAM and 15-20 mg $CdCl_2$ were loaded into a 25 mL flask and degassed under vacuum at 120 °C. After the evolution of bubbles stopped (approximately 20 minutes), the flask was switched to an argon atmosphere (maintained using a Schlenk line) and heated to 230 °C. Once the temperature stabilized, 265 nmols of small CdS seed NCs (2-4 nm diameter) were swiftly injected into the flask and left to coalesce for 60 minutes. The flask was then removed from the heating mantle and quenched in a water bath. The NCs were cleaned via precipitation with toluene/ethanol mixture, twice. The final NCs were suspended in hexane and stored under ambient conditions.

Colloidal-epitaxy synthesis of CdS_{bulk}-CdSe core-shell NCs. The formation of the CdSe emitting shell layer onto CdS core NCs was done by injection of two precursors (0.1 M Cd-oleate and 0.1 M TOP-Se, not mixed) *via* a syringe pump. The Cd-oleate precursor was prepared by adding 206 mg CdO, 4 mL OA, and 12 mL ODE into a 50 mL flask and heating to 260 °C under argon until a clear and nearly colorless solution was obtained. The Se precursor was made by combining 47 mg Se powder and 1 mL TOP into a 10 mL flask and heating to 150 C under argon until all the selenium powder had reacted, then 5 mL of ODE was added to the flask to dilute the solution. To begin, 40-100 nmols of CdS NCs were loaded into a 50 mL flask with 2 mL OLAM and 2 mL ODE, placed under argon (*via* a Schlenk line) and the temperature was set to 320 °C. At 260 °C the CdSe precursors began to be injected into the flask at a rate of 3 mL/hr. The injection was allowed to continue until the emission had reached the desired wavelength (usually anywhere from 630 nm to 680 nm). Once the injection was stopped, the reaction was annealed for 30 minutes and then removed from the heating mantle and left to cooled to room temperature. The solution

was cleaned by precipitation with toluene and 2:1 ethanol acetone mixture. The final NCs were suspended in hexane.

Synthesis of CdS_{bulk}-CdSe-CdS core-shell-shell NCs. The growth of CdS shell layer was adapted from literature.[64] $Cd(oleate)_2$ and octanethiol were used as the Cd and S precursors, respectively. The $Cd(oleate)_2$ solution used was the same as for the CdSe layer. The octanethiol solution was prepared by mixing 12 mL ODE and 0.25 mL octanethiol. The 40 nmols of CdS/CdSe prepared previously were loaded into a 50 mL flask with 2 mL OLAM and 2 mL ODE. The flask was degassed at 120 °C, then placed under argon and heated to 320 °C. In separate syringe pumps, the two precursors were injected at 3 mL/hr beginning at approximately 300 °C. The reaction was stopped once the desired shell thickness was reached, typically 3-4 hours. Once the injection was finished, the solution was left to anneal for 30 minutes before being removed from the hear and allowed to cool to room temperature. NCs were then cleaned by 3 precipitations with toluene/ethanol *via* centrifugation. The final NCs were dispersed in hexane.

Characterization. Absorbance spectra were acquired using a Cary 60 scan spectrophotometer. Photoluminescence (PL) spectra were measured by excitation with a pulsed 405 nm laser diode (PDL 800-D, Picoquant) and emitted photons were collected by a fiber optic cable connected to an Andor Shamrock 303i spectrograph and measured using an Andor Newton 970 EMCCD. PL decay dynamics were acquired via 405 nm pulsed excitation (picoquant) and photons were detected with an ID100-50 single photon detector (ID Quantique) and processed by a SPC-130 TCSPC module (Becker & Hickl). Transmission electron microscope (TEM) images were acquired at 200 kV on carbon films coated with a copper grid (300 mesh, obtained from Electron Microscope Science) using a Thermo Fisher Talos F200X G2 S/TEM. Relative quantum yield (QY) measurements were acquired with a 532 nm CW DPSS laser (MeshTel INTELITE, INC. USA) and R101 dye was used as a reference (99% QY in ethanol).

Amplified Spontaneous Emission Measurements and Dynamics. Nanocrystal thin-films were fabricated by first performing an additional anti-solvent precipitation with ethanol, followed by redispersion in a 9:1 hexane/octane mixture. Concentrated solutions were drop-cast onto microscope slides that had been treated with MPTS over 24 hours (5% MPTS w/v in dried toluene). The samples with showed the lowest ASE thresholds were spin coated at 2000 rpm. Samples that displayed the best ASE results were opalescent, non-scattering; other films however, displayed

perceptible haze. Samples were photoexcited with a 35 fs Ti:sapphire laser (2 kHz, Spectraphysics), which was frequency doubled to 400 nm. The 400 nm beam was focused using a cylindrical lens to produced a strip, with the edges defined by razor blades. The emission was collected via a lens positioned perpendicular to the excitation beam and fiber-coupled to a CCD through a monochromater (Princeton), for spectral data acquisition, or to a streak camera (Hamamatsu) for time-resolved data collection.

Fluorescence Correlation Spectroscopy. We detect emission from diffusing QDs in solution, under a confocal microscope and using a pulsed excitation source in a Hanbury-Brown-Twiss setup, and calculate the second order cross-correlation function, $g(2)(\tau)$. In the case of solution-based measurements, this is also known as Fluorescence Correlation Spectroscopy (FCS). At early τ, before QDs have diffused out of the confocal volume being probed, photon pairs are more likely to emit from the same QD, thereby causing $g(2)(\tau)$ to have a higher degree of correlation at timescales faster than the diffusion time of the QDs. For large τ, beyond the diffusion time, photon pairs are highly unlikely to originate from the same QD, and $g(2)(\tau)$ consists of uncorrelated photon pairs from the ensemble. At $\tau=0$, the intensity is a mixture of antibunching from exciton emission, bunching from biexciton emission and some signal from photon pairs from different QDs. For a dilute sample with a high degree of correlation at short time scales (small τ), we can subtract the uncorrelated ensemble emission (large τ) to isolate the correlations from single QDs. We determine the ensemble averaged BX/X QY by taking the ratio of the ensemble background subtracted correlation center peak ($g^{(2)}(0)$-1) to the correlation side peak ($g^{(2)}(\tau_{rep})$-1), where τ_{rep} is the repetition rate of the laser. The correlation side peak is determined by fitting correlations across all timescales to a 2D diffusion model (the Supporting Information). All measurements were performed under low excitation flux ($\langle n \rangle \ll 1$) in order to avoid emission from higher order multiexcitons. Additionally, we ensured that the repetition rate of the pulsed laser was well beyond the lifetime of the emitter.

Acknowledgment. This work was supported by the Award DE-SC0016872 (MZ) funded by the U.S. Department of Energy, Office of Science. The authors acknowledge the financial support of the University of Michigan College of Engineering and NSF grant #DMR-9871177, and technical support from the Michigan Center for Materials Characterization. DB and AP were supported by the U.S.

Department of Energy, Office of Science, Basic Energy Sciences under Award DE-SC0021650. This work was performed, in part, at the Center for Nanoscale Materials, a U.S. Department of Energy Office of Science User Facility, and supported by the U.S. Department of Energy, Office of Science, under Contract No. DE-AC02-06CH11357 . Work of UT Dallas group (AVM, Navendu Mondal (NM) and Kehui Zhang (KZ)) was supported by DOE-BES award #DE-SC0010697.

Supporting information. Additional figures, including TEM and STEM images, PL QY calculations, single-particle PL dynamics, and high-power ASE measurements. Experimental procedures section. Model calculations of the e-h overlap and the exciton-exciton binding energy.

References

[1] Park, Y.-S.;, Roh, J., .; Diroll, B. T., .; Schaller, R. D.; & Klimov, V. I. Colloidal quantum Quantum dot Dot lasersLasers. *Nat. Rev. Mater.* **2021**, *6*, 382–401 2021.

[2] Shirasaki, Y., Supran, G. J., Bawendi, M. G. & Bulović, V. Emergence of colloidal Colloidal quantumQuantum-dot Dot lightLight-emitting Emitting technologiesTechnologies. *Nat.ure Photonics* **2013**, *7*, 13–23 2013.

[3] Hanifi, D. A.; Bronstein, N. D.; Koscher, B. A.; Nett, Z.; Swabeck, J. K.; Takano, K.; Schwartzberg, A. M.; Maserati, L.; Vandewal, K.; van de Burgt, Y.; Salleo, A.; Alivisatos, A. P. Redefining Near-Unity Luminescence in Quantum Dots with Photothermal Threshold Quantum Yield. *Science* **2019**, *363*, 1199–1202.

[4] Yang, J.; Choi, M. K.; Yang, U. J.; Kim, S. Y.; Kim, Y. S.; Kim, J. H.; Kim, D.-H.; Hyeon, T. Toward Full-Color Electroluminescent Quantum Dot Displays. *Nano Lett.* **2021**, *21*, 26–33.

[5] Panfil, Y. E.; Oded, M.; Banin, U. Colloidal Quantum Nanostructures: Emerging Materials for Display Applications. *Angew. Chem. Int. Ed.* **2018**, *57*, 4274–4295.

[6] García de Arquer, F. P.; Talapin, D. V.; Klimov, V. I.; Arakawa, Y.; Bayer, M.; Sargent, E. H. Semiconductor quantum dots: Technological Progress and Future Challenges. *Science* **2021**, 373, eaaz8541.

[7] Lim, J.; Park, Y.-S.; Klimov, V. I. Optical Gain in Colloidal Quantum Dots Achieved with Direct-Current Electrical Pumping. *Nat. Mater.* **2018**, *17*, 42–49.

[8] Wang, Y.; Sun, H. Advances and Prospects of Lasers Developed from Colloidal Semiconductor Nanostructures. *Prog. Quantum. Electron.* **2018**, *60*, 1–29.

[9] Yakunin, S.; Protesescu, L.; Krieg, F.; Bodnarchuk, M. I.; Nedelcu, G.; Humer, M.; De Luca, G.; Fiebig, M.; Heiss, W.; Kovalenko, M. V. Low-Threshold Amplified Spontaneous Emission and Lasing from Colloidal Nanocrystals of Caesium Lead Halide Perovskites. *Nat. Commun.* **2015**, *6*, 8056.

[10] Fan, F.; Voznyy, O.; Sabatini, R. P.; Bicanic, K. T.; Adachi, M. M.; McBride, J. R.; Reid, K. R.; Park, Y.-S.; Li, X.; Jain, A.; Quintero-Bermudez, R.; Saravanapavanantham, M.; Liu, M.; Korkusinski, M.; Hawrylak, P.; Klimov, V. I.; Rosenthal, S. J.; Hoogland, S.; Sargent, E. H. Continuous-Wave Lasing in Colloidal Quantum Dot Solids Enabled by Facet-Selective Epitaxy. *Nature* **2017**, *544*, 75–79.

[11] Yang, Z.; Pelton, M.; Fedin, I.; Talapin, D. V.; Waks, E. A. Room Temperature Continuous-Wave Nanolaser Using Solloidal Quantum Wells. *Nat. Commun.* **2017**, *8*, 143.

[12] Kazes, M.; Lewis, D.; Ebenstein, Y.; Mokari, T.; Banin, U. Lasing from Semiconductor Quantum Rods in a Cylindrical Microcavity. *Adv. Mater*. **2002**, *14*, 317–321.

[13] Wang, Y.; Fong, K. E.; Yang, S.; Ta, V. D.; Gao, Y.; Wang, Z.; Nalla, V.; Demir, H. V.; Sun, H. Unraveling the Ultralow Threshold Stimulated Emission from CdZnS/ZnS Quantum Dot and Enabling High-Q Microlasers. *Laser Photonics. Rev.* **2015**, *9*, 507–516.

[14] Dai, X.; Deng, Y.; Peng, X.; Jin, Y. Quantum-Dot Light-Emitting Diodes for Large-Area Displays: Towards the Dawn of Commercialization. *Adv. Mater.* **2017**, *29*, 1607022.

[15] Azzellino, G.; Freyria, F. S.; Nasilowski, M.; Bawendi, M. G.; Bulović, V. Micron-Scale Patterning of High Quantum Yield Quantum Dot LEDs. *Adv. Mater. Technol*. **2019**, *4*, 1800727.

[16] Roh, J.; Park, Y.-S.; Lim, J.; Klimov, V. I. Optically Pumped Colloidal-Quantum-Dot Lasing in LED-Like Devices with an Integrated Optical Cavity. *Nat. Commun.* **2020**, *11*, 1–10.

[17] Bae, W. K.; Park, Y.-S.; Lim, J.; Lee, D.; Padilha, L. A.; McDaniel, H.; Robel, I.; Lee, C.; Pietryga, J. M.; Klimov, V. I. Controlling the Influence of Auger Recombination on the Performance of Quantum-Dot Light-Emitting Diodes. *Nat. Commun.* **2013**, *4*, 2661.

[18] Klimov, V. I.; Mikhailovsky, A. A.; McBranch, D. W.; Leatherdale, C. A.; Bawendi, M. G. Quantization of Multiparticle Auger Rates in Semiconductor Quantum Dots. *Science* **2000**, *287*, 1011–1013.

[19] Kharchenko, V. A.; Rosen, M. Auger Relaxation Processes in Semiconductor Nanocrystals and Quantum Wells. *J. Lumin.* **1996**, *70*, 158–169.

[20] Ben-Shahar, Y.; Philbin, J. P.; Scotognella, F.; Ganzer, L.; Cerullo, G.; Rabani, E.; Banin, U. Charge Carrier Dynamics in Photocatalytic Hybrid Semiconducto-Metal Nanorods: Crossover from Auger Recombination to Charge Transfer. *Nano Lett.* **2018**, *18*, 5211–5216.

[21] She, C.; Fedin, I.; Dolzhnikov, D. S.; Demortière, A.; Schaller, R. D.; Pelton, M.; Talapin, D. V. Low-Threshold Stimulated Emission Using Colloidal Quantum Wells. *Nano Lett.* **2014**, *14*, 2772–2777.

[22] Kelestemur, Y.; Shynkarenko, Y.; Anni, M.; Yakunin, S.; De Giorgi, M. L.; Kovalenko, M. V. Colloidal CdSe Quantum Wells with Graded Shell Composition for Low-Threshold Amplified Spontaneous Emission and Highly Efficient Electroluminescence. *ACS Nano* **2019**, *13*, 13899–13909.

[23] Guzelturk, B.; Pelton, M.; Olutas, M.; Demir, H. V. Giant Modal Gain Coefficients in Colloidal II-VI Nanoplatelets. *Nano Lett.* **2019**, *19*, 277–282.

[24] Chen, B.; Chang, S.; Li, D.; Chen, L.; Wang, Y.; Chen, T.; Zou, B.; Zhong, H.; Rogach, A. L. Template Synthesis of $CuInS_2$ Nanocrystals from In_2S_3 Nanoplates and Their Application as Counter Electrodes in Dye-Sensitized Solar Cells. *Chem. Mater.* **2015**, *27*, 5949–5956.

[25] García-Santamaría, F.; Chen, Y.; Vela, J.; Schaller, R. D.; Hollingsworth, J. A.; Klimov, V. I. Suppressed Auger Recombination in "Giant" Nanocrystals Boosts Optical Gain Performance. *Nano Lett*. **2009**, *9*, 3482–3488.

[26] Lin, C. H.; Lafalce, E.; Jung, J.; Smith, M. J.; Malak, S. T.; Aryal, S.; Yoon, Y. J.; Zhai, Y.; Lin, Z.; Vardeny, Z. V.; Tsukruk, V. V. Core/Alloyed-Shell Quantum Dot Robust Solid Films with High Optical Gains. *ACS Photonics* **2016**, *3*, 647–658.

[27] Hou, X.; Qin, H.; Peng, X. Enhancing Dielectric Screening for Auger Suppression in CdSe/CdS Quantum Dots by Epitaxial Growth of ZnS Shell. *Nano Lett.* **2021**, *21*, 3871–3878.

[28] Razgoniaeva, N.; Moroz, P.; Yang, M.; Budkina, D. S.; Eckard, H.; Augspurger, M.; Khon, D.; Tarnovsky, A. N.; Zamkov, M. One-Dimensional Carrier Confinement in "Giant" CdS/CdSe Excitonic Nanoshells. *J. Am. Chem. Soc*. **2017**, *139*, 7815–7822.

[29] Kholmicheva, N.; Budkina, D. S.; Cassidy, J.; Porotnikov, D.; Harankahage, D.; Boddy, A.; Galindo, M.; Khon, D.; Tarnovsky, A. N.; Zamkov, M. Sustained Biexciton Populations in Nanoshell Quantum Dots. *ACS Photonics* **2019**, *6*, 1041–1050.

[30] Nagamine, G.; Jeong, B. G.; Ferreira, T. A. C.; Chang, J. H.; Park, K.; Lee, D. C.; Bae, W. K.; Padilha, L. A. Efficient Optical Gain in Spherical Quantum Wells Enabled by Engineering Biexciton Interactions. *ACS Photonics* **2020**, *7*, 2252-2264.

[31] Porotnikov, D.; Diroll, B. T.; Harankahage, D.; Obloy, L.; Yang, M.; Cassidy, J.; Ellison, C.; Miller, E.; Rogers, S.; Tarnovsky, A. N.; Schaller, R. D.; Zamkov, M. Low-Threshold Laser Medium Utilizing Semiconductor Nanoshell Quantum Dots. *Nanoscale* **2020**, *12*, 17426–17436.

[32] Cassidy, J.; Zamkov, M. Nanoshell Quantum Dots: Quantum Confinement Beyond the Exciton Bohr Radius. *J. Chem. Phys.* **2020**, *152*, 110902.

[33] Klimov, V. I.; Ivanov, S. A.; Nanda, J.; Achermann, M.; Bezel, I.; McGuire, J. A.; Piryatinski, A. Single-Exciton Optical Gain in Semiconductor Nanocrystals. *Nature* **2007**, *447*, 441–446.

[34] Ivanov, S. A.; Nanda, J.; Piryatinski, A.; Achermann, M.; Balet, L. P.; Bezel, I. V.; Anikeeva, P. O.; Tretiak, S.; Klimov, V. I. Light Amplification Using Inverted Core/Shell Nanocrystals: Towards Lasing in the Single-Exciton Regime. *J. Phys. Chem. B* **2004**, *108*, 10625–10630.

[35] Dang, C.; Lee, J.; Breen, C.; Steckel, J. S.; Coe-Sullivan, S.; Nurmikko, A. Red, Green and Blue Lasing Enabled by Single-Exciton Gain in Colloidal Quantum Dot Films. *Nat. Nanotechnol.* **2012**, *7*, 335–339.

[36] Pokatilov, E. P.; Fonoberov, V. A.; Fomin, V. M.; Devreese, J. T. Electron and Hole States in Quantum Dot Quantum Wells within a Spherical Eight-Band Model. *Phys. Rev. B* **2001**, *64*, 245329.

[37] Dias, E. A.; Saari, J. I.; Tyagi, P.; Kambhampati, P. Improving Optical Gain Performance in Semiconductor Quantum Dots *via* Coupled Quantum Shells. *J. Phys. Chem. C* **2012**, *116*, 5407–5413.

[38] Braun, M.; Link, S.; Burda, C.; El-Sayed, M. Transfer Times of Electrons and Holes across the Interface in CdS/HgS/CdS Quantum Dot Quantum Well Nanoparticles. *Chem. Phys. Lett.* **2002**, *361*, 446–452.

[39] Xu, J.; Xiao, M. Lasing Action in Colloidal CdS/CdSe/CdS Quantum Wells. *Appl. Phys. Lett.* **2005**, *87*, 173117.

[40] Xu, J.; Xiao, M.; Battaglia, D.; Peng, X. Exciton Radiative Recombination in Spherical CdS⁄CdSe⁄CdS Quantum-Well Nanostructures. *Appl. Phys. Lett.* **2005**, *87*, 043107.

[41] Battaglia, D.; Li, J. J.; Wang, Y.; Peng, X. Colloidal Two-Dimensional Systems: CdSe Quantum Shells and Wells. *Angew. Chem. Int. Ed.* **2003**, *42*, 5035–5039.

[42] Jeong, B. G.; Park, Y.-S.; Chang, J. H.; Cho, I.; Kim, J. K.; Kim, H.; Char, K.; Cho, J.; Klimov, V. I.; Park, P.; Lee, D. C.; Bae, W. K. Colloidal Spherical Quantum Wells with Near-Unity Photoluminescence Quantum Yield and Suppressed Blinking. *ACS Nano* **2016**, *10*, 9297–9305.

[43] Philbin, J. P.; Rabani, E. Electron-Hole Correlations Govern Auger Recombination in Nanostructures. *Nano Lett.* **2018**, *18*, 7889–7895.

[44] Robel, I.; Gresback, R.; Kortshagen, U.; Schaller, R. D.; Klimov, V. I. Universal Size-Dependent Trend in Auger Recombination in Direct-Gap and Indirect-Gap Semiconductor Nanocrystals. *Phys. Rev. Lett.* **2009**, *102*, 177404.

[45] Kurian, P. A.; Vijayan, C.; Sathiyamoorthy, K.; Suchand Sandeep, C. S.; Philip, R. Excitonic Transitions and Off-resonant Optical Limiting in CdS Quantum Dots Stabilized in a Synthetic Glue Matrix. *Nanoscale Res. Lett.* **2007**, *2*, 561–568.

[46] Beyler, A. P.; Bischof, T. S.; Cui, J.; Coropceanu, I.; Harris, D. K.; Bawendi M. G. Sample-Averaged Biexciton Quantum Yield Measured by Solution-Phase Photon Correlation. *Nano Lett.* **2014**, *14*, 6792–6798.

[47] Park, Y-S.; Malko, A. V.; Vela, J.; Chen, Y.; Ghosh, Y.; Garcia-Santamaria, F.; Hollingsworth, J. A.; Klimov, V. I.; Htoon, H. Near-Unity Quantum Yields of Biexciton Emission from CdSe/CdS Nanocrystals Measured Using Single-Particle Spectroscopy. *Phys. Rev. Lett.* **2011**, *106*, 187401.

[48] Klimov, V. I.; Mikhailovsky, A.A.; Xu, S.; Malko, A. V.; Hollingsworth, J. A.; Leatherdale, C. A.; Eisler, H.; Bawendi, M. G. Optical Gain and Stimulated Emission in Nanocrystal Quantum Dots. *Science* **2000**, *290*, 314–317.

[49] Malko, A. V.; Mikhailovsky, A. A.; Petruska, M. A.; Hollingsworth, J. A.; Htoon, H.; Bawendi, M. G.; Klimov, V. I. From Amplified Spontaneous Emission to Microring Lasing Using Nanocrystal Quantum Dot Solids. *Appl. Phys. Lett.* **2002**, *81*, 1303–1305.

[50] Mikhailovsky, A. A.; Malko, A. V.; Hollingsworth, J. A.; Bawendi, M. G.; Klimov, V. I. Multiparticle Interactions and Stimulated Emission in Chemically Synthesized Quantum Dots. *Appl. Phys. Lett.* **2002**, *80*, 2380–2382.

[51] Taghipour, N.; Delikanli, S.; Shendre, S.; Sak, M.; Li, M.; Isik, F.; Tanriover, I.; Guzelturk, B.; Sum, T. C.; Demir, H. V. Sub-Single Exciton Optical Gain Threshold in Colloidal Semiconductor Quantum Wells with Gradient Alloy Shelling. *Nat. Commun.* **2020**, *11*, 3305.

[52] Kozlov, O. V.; Park, Y.-S.; Roh, J.; Fedin, I.; Nakotte, T.; Klimov, V. I. Sub-Single-Exciton Lasing Using Charged Quantum Dots Coupled to a Distributed Feedback Cavity. *Science* **2019**, *365*, 672–675.

[53] Cooney, R. R.; Sewall, S. L.; Sagar, D. M.; Kambhampati, P. Gain Control in Semiconductor Quantum Dots *via* State-Resolved Optical Pumping. *Phys. Rev. Lett*. **2009**, *102*, 127404.

[54] Kambhampati, P. Multiexcitons in Semiconductor Nanocrystals: A Platform for Optoelectronics at High Carrier Concentration. *J. Phys. Chem. Lett.* **2012**, *3*, 1182.

[55] Kambhampati, P.; Mack, T.; Jethi, L. Understanding and Exploiting the Interface of Semiconductor Nanocrystals for Light Emissive Applications. *ACS Photonics* **2017**, *4*, 412–423.

[56] Walsh, B. R.; Saari, J. I.; Krause, M. M.; Mack, T. G.; Nick, R.; Coe-Sullivan, S.; Kambhampati, P. Interfacial Electronic Structure in Graded Shell Nanocrystals Dictates Their Performance for Optical Gain. *J. Phys. Chem. C* **2016**, *120*, 19409–19415.

[57] Dias, E. A.; Saari, J. I.; Tyagi, P.; Kambhampati, P. Improving Optical Gain Performance in Semiconductor Quantum Dots via Coupled Quantum Shells. *J. Phys. Chem. C* **2012**, *116*, 5407–5413.

[58] Kobiyama, E.; Tahara, H.; Sato, R.; Saruyama, M.; Teranishi, T.; Kanemitsu, Y. Reduction of Optical Gain Threshold in $CsPbI_3$ Nanocrystals Achieved by Generation of Asymmetric Hot-Biexcitons. *Nano Lett.* **2020**, *20*, 3905–3910.

[59] Haus, J. W.; Zhou, H. S.; Honma, I.; Komiyama, H. Quantum Confinement in Semiconductor Heterostructure Nanometer-Size Particles. *Phys. Rev. B* **1993**, *47*, 1359–1365.

[60] Sahu, A.; Kumar, D. Theoretical Modeling of a "Giant" Colloidal Core-Shell Quantum Dot with an Alloyed Interfacial Layer for Solar Cell Applications. *J. Opt. Soc. Am. B* **2021**, *38*, 842.

[61] Piryatinski, A.; Ivanov, S. A.; Tretiak, S.; Klimov, V. I. Effect of Quantum and Dielectric Confinement on the Exciton-Exciton Interaction Energy in Type II Core/Shell Semiconductor Nanocrystals. *Nano Lett.* **2007**, *7*, 108–115.

[62] Yu, W. W.; Peng, X. Formation of High-Quality CdS and Other II-VI Semiconductor Nanocrystals in Noncoordinating Solvents: Tunable Reactivity of Monomers. *Angew. Chem.* **2002**, *114*, 2474−2477.

[63] Cassidy, J.; Ellison, C.; Bettinger, J.; Yang, M.; Moroz, P.; Zamkov, M. Enabling Narrow Emission Linewidths in Colloidal Nanocrystals through Coalescence Growth. *Chem. Mater.* **2020**, *32*, 7524–7534.

[64] Chen, O.; Zhao, J.; Chauhan, V. P.; Cui, J.; Wong, C.; Harris, D. K.; Wei, H.; Han, H.-S.; Fukumura, D.; Jain, R. K.; Bawendi, M. G. Compact High-Quality CdSe-CdS Core-Shell Nanocrystals with Narrow Emission Linewidths and Suppressed Blinking. *Nat. Mater.* **2013**, *12*, 445–451.